UC Irvine
UC Irvine Previously Published Works

Title

Regulatory T cells suppress Th17 cell Ca2+ signaling in the spinal cord during murine autoimmune neuroinflammation

Permalink

Journal

ISSN

Authors

Othy, Shivashankar
Jairaman, Amit
Dynes, Joseph L
et al.

Publication Date

DOI

Peer reviewed

Regulatory T cells suppress Th17 cell Ca²⁺ signaling in the spinal cord during murine autoimmune neuroinflammation

Shivashankar Othy[a,1,2] , Amit Jairaman[a,1] , Joseph L. Dynes[a], Tobias X. Dong[a], Cornelia Tune[a,3], Andriy V. Yeromin[a], Angel Zavala[a], Chijioke Akunwafo[a], Fangyi Chen[a] , Ian Parker[a,b], and Michael D. Cahalan[a,c,2]

[a]Department of Physiology & Biophysics, University of California, Irvine, CA 92697; [b]Department of Neurobiology & Behavior, University of California, Irvine, CA 92697; and [c]Institute for Immunology, University of California, Irvine, CA 92697

T lymphocyte motility and interaction dynamics with other immune cells are vital determinants of immune responses. Regulatory T (Treg) cells prevent autoimmune disorders by suppressing excessive lymphocyte activity, but how interstitial motility patterns of Treg cells limit neuroinflammation is not well understood. We used two-photon microscopy to elucidate the spatial organization, motility characteristics, and interactions of endogenous Treg and Th17 cells together with antigen-presenting cells (APCs) within the spinal cord leptomeninges in experimental autoimmune encephalomyelitis (EAE), an animal model of multiple sclerosis. Th17 cells arrive before the onset of clinical symptoms, distribute uniformly during the peak, and decline in numbers during later stages of EAE. In contrast, Treg cells arrive after Th17 cells and persist during the chronic phase. Th17 cells meander widely, interact with APCs, and exhibit cytosolic Ca²⁺ transients and elevated basal Ca²⁺ levels before the arrival of Treg cells. In contrast, Treg cells adopt a confined, repetitive-scanning motility while contacting APCs. These locally confined but highly motile Treg cells limit Th17 cells from accessing APCs and suppress Th17 cell Ca²⁺ signaling by a mechanism that is upstream of store-operated Ca²⁺ entry. Finally, Treg cell depletion increases APC numbers in the spinal cord and exaggerates ongoing neuroinflammation. Our results point to fundamental differences in motility characteristics between Th17 and Treg cells in the inflamed spinal cord and reveal three potential cellular mechanisms by which Treg cells regulate Th17 cell effector functions: reduction of APC density, limiting access of Th17 cells to APCs, and suppression of Th17 Ca²⁺ signaling.

regulatory T cell | Th17 cell | neuroinflammation | two-photon immunoimaging | calcium signaling

Regulatory T (Treg) cells expressing the transcription factor forkhead box protein P3 (Foxp3) maintain peripheral immune tolerance. Several autoimmune and inflammatory pathologies in humans are associated with functional defects in Treg cells, and selective depletion of Treg cells in experimental animals leads to systemic autoimmune disease and unchecked lymphoproliferation (1). Conversely, adoptively transferred Treg cells limit the pathogenicity in animal models of autoimmunity (2). Furthermore, Treg-based adoptive cell therapies for autoimmune diseases and for induction and maintenance of tolerance following transplantation are being developed in humans, leading to numerous clinical trials (3, 4). Despite these advances, the underlying cellular and molecular mechanisms by which Treg cells limit damage in autoimmune disease are not fully understood.

A thorough characterization of the in situ cellular interactions of endogenous Treg cells with effector T cells and antigen-presenting cells (APCs) would provide important insights toward a mechanistic understanding of immunoregulation, and may suggest therapeutic treatment modalities for autoimmunity. Both soluble factors and direct contact between cells have been implicated in Treg-mediated suppression (5). Th17 cells are associated

with several autoimmune and systemic inflammatory diseases, and are considered to be the main pathogenic cells in the experimental autoimmune encephalomyelitis (EAE) murine model of multiple sclerosis (6, 7). However, no studies have yet tracked associations between endogenous Th17 and Treg cells in relation to APCs within the complex inflammatory tissue environment.

A well-established signal transduction pathway links TCR binding of peptide-MHC on APCs to proximal signaling events leading to generation of IP₃ and consequent depletion of Ca²⁺ from the endoplasmic reticulum (ER), mobilization of ER STIM1 proteins to ER–PM junctions, and triggering of Ca²⁺ influx through Ca²⁺-selective Orai1 channels in a process termed "store-operated Ca²⁺ entry" (SOCE) (8, 9). Sustained cytosolic Ca²⁺ signaling activates calcineurin- and NFAT-mediated gene expression to drive cytokine production, cellular differentiation, and proliferation in T cells (10, 11). In addition, cytosolic Ca²⁺ elevation rapidly inhibits T cell motility (12, 13), underlying the "stop" signal that anchors T cells to an APC as the immunological synapse forms. The central role of

Significance

Regulatory T (Treg) cells mediate immune homeostasis, aid in tissue repair, and resolve inflammation in numerous autoimmune diseases; however, little is known about the role of Treg cell motility dynamics in immunoregulation. We imaged the organization and motility patterns of endogenous Treg cells in the spinal cord together with pathogenic Th17 cells in a mouse model of neuroinflammation. Treg cells exhibit repetitive-scanning motility, which may be important in suppressing Th17 cell effector functions by inhibition of Ca²⁺ signaling and by limiting their access to APCs, thus limiting their reactivation in the spinal cord. These findings will help to understand how Treg cells prevent autoimmunity and dampen immune responses, and how autoimmune diseases can be effectively targeted using Treg-based cellular therapies.

See online for related content such as Commentaries.

[1]S.O. and A.J. contributed equally to this work.

[2]To whom correspondence may be addressed. Email: mcahalan@uci.edu or sothy@uci.edu.

[3]Present address: Institut für Anatomie, Universität zu Lübeck, 23562 Lübeck, Germany.

Ca^{2+} signaling in T cell activation evoked by T cell receptor (TCR) engagement during antigen recognition is well established (14), and recent studies have identified Orai1 Ca^{2+} signaling in Th17 cells as a critical regulator of encephalitogenicity in EAE (15, 16). Previous reports on lymphocyte Ca^{2+} signaling in the EAE model used adoptively transferred TCR transgenic T cells that were virally transduced with a FRET-based genetically encoded Ca^{2+} indicator (17, 18). However, the dynamics of Ca^{2+} signaling in endogenous Th17 cells during EAE have not been studied to our knowledge.

In this report, we use two-photon microscopy to comprehensively analyze the dynamics and functional interactions of endogenous Treg cells with APCs and encephalitogenic Th17 cells in the spinal cord during the onset, peak, and chronic phases of autoimmune neuroinflammation in the MOG-EAE model. Our approach included development of dual-reporter mouse strains expressing cell type-specific green or red fluorescent proteins to simultaneously visualize the motility and interaction dynamics of endogenous Treg and Th17 cells within the spinal leptomeninges. We report that Treg cells are rapidly motile but relatively confined, in contrast to the fast, meandering motility of Th17 cells. We identify a repetitive scanning Treg cell behavior that may limit access of Th17 cells to APCs. By expressing Salsa6f, a ratiometric genetically encoded Ca^{2+} indicator (19), in endogenous Th17 cells, we demonstrate that Treg infiltration is associated with diminished Ca^{2+} signaling in Th17 cells. Finally, we show that Treg cells directly suppress TCR-induced Ca^{2+} signaling in Th17 cells without affecting the machinery for SOCE.

Results

Spatial Organization of Endogenous Treg and Th17 Cells during Onset, Peak, and Chronic Phases of EAE in the Leptomeninges. To study Treg and Th17 cellular dynamics and interactions in the spinal cord, we developed Foxp3^{EGFP} IL-17^{TdT} dual-reporter mice in which EGFP is expressed in endogenous Treg cells and TdTomato in Th17 cells. Following s.c. injection of myelin oligodendrocyte glycoprotein peptide (MOG$_{35-55}$) with adjuvant (20, 21), EAE was induced, resulting in an ascending paralysis and clinical scores of increasing severity. To obtain "snapshots" of the cellular distribution throughout the cord, spinal cords were isolated and fixed from dual-reporter mice at onset, peak, and chronic phases of EAE, and then imaged using two-photon microscopy (*SI Appendix*, Fig. S1 *A* and *B*). Flow cytometry analysis showed that less than 1% of CD4 T cells are double-positive for GFP (green) and TdTomato (red) in the spinal cord of EAE mice (*SI Appendix*, Fig. S1C), strongly suggesting that Th17 cells do not acquire FoxP3 expression, consistent with a previous fate-mapping study (22). By tiling individual 3D volumes, we formed composite images along the entire cord, visualizing endogenous Treg cells (green) and Th17 cells (red) together with collagen fibers (blue) in the ventral leptomeninges where plaques are more numerous (23) (Fig. 1).

At the onset of EAE, ~10 days postimmunization (DPI), Th17 cells were primarily found in the lumbar region (Fig. 1A and Movie S1). This region contained very few Treg cells, which were located in the vicinity of Th17 cells (Fig. 1B). Autofluorescent bodies (yellow), indicative of regions of macrophage/microglial activation (24), were present but rare. Cell counts showed that Th17 and Treg cells were primarily localized at 21 to 25 mm along the rostral–caudal axis from the brainstem, and Th17 cells greatly outnumbered Treg cells at this early phase of disease (Fig. 1C). These results show that the initial sites of neuroinflammation in the CNS during EAE are within the lumbar leptomeninges, corresponding to the initial clinical sign of tail paralysis. We also examined the choroid plexus at the onset of EAE, but detected very few Th17 cells and no Treg cells in the fourth ventricle at the onset of EAE (*SI Appendix*, Fig. S1D). These findings are in agreement with previous studies, which showed that adoptively transferred autoreactive T cells enter the CNS at the lumbar (L5) spinal cord and are primarily localized in

the leptomeninges, but not in the choroid plexus (25, 26). During the peak phase of EAE, at ~21 DPI, Treg and Th17 cells were found along the entire length of the spinal cord (Fig. 1 *D–F* and Movie S2). At this time, autofluorescence indicative of macrophage/microglial activation was uniformly high throughout the length of cord, and both Th17 and Treg numbers were increased, with Th17 cells still outnumbering Treg cells. Infiltration of Th17 cells into the rostral portion of the spinal cord coincided with the rostral progression of paralysis from tail to forelimbs. During the chronic phase of EAE, after 28 DPI, numbers of Th17 cells were notably lower than at the peak, while the numbers of Treg cells remained elevated (Fig. 1 *G–I* and Movie S3). The intensity of autofluorescence was higher than during the peak phase, implying the formation of tertiary lymphoid structures (TLS) common in chronic inflammatory conditions (27, 28). The decrease in Th17 cell numbers was most prominent in the rostral cord, coinciding with functional recovery from forelimb paralysis, whereas the persistence of Th17 cells and high autofluorescence in the lumbar region coincided with continued hind limb and tail paralysis, although with partial functional recovery.

To validate our findings in a nontransgenic model, we induced EAE in C57BL6J WT mice and used flow cytometry to analyze the number of Treg and Th17 cells by antibody staining for Foxp3 and IL-17, respectively. Consistent with the imaging data and a previous report (29), the numbers of Th17 cells in the brain and spinal cord were highest at the peak of the disease and diminished at 28 DPI, while Treg cells showed a progressive increase during the course of EAE (*SI Appendix*, Fig. S1E).

In summary, Th17 cells are primarily localized to the lumbar region at onset of EAE, increase in numbers and spread along the entire spinal cord at the peak, and then decline in numbers during the chronic phase. Treg cells subsequently infiltrate the spinal cord and are maintained during the chronic phase. These results document EAE-dependent changes in endogenous Th17 and Treg cell distributions in the spinal cord and provide a guide for identifying cell behaviors that promote or restrain inflammation during EAE.

Treg Cells Display Rapid but Confined Motility in Leptomeninges, Distinct from Th17 Cells. In parallel with fixed spinal cord imaging to determine cellular localization described above, we used live two-photon microscopy to study Th17 and Treg cell dynamics in explanted spinal cords from Foxp3^{EGFP} IL-17^{TdT} reporter mice undergoing EAE. At 21 DPI, both Treg and Th17 cells actively, but independently, explored networks of collagen fibers (blue) in the leptomeninges, displaying amoeboid migration with elongated uropods (Fig. 2A and Movie S4). An overlay of cell tracks showed that, whereas Treg movements are relatively constrained, Th17 cells spread more extensively (Fig. 2 *B* and *C*). Despite similar distributions of instantaneous 3D velocities (Fig. 2D), comparisons of mean square displacement (MSD) plots and average motility coefficients revealed that Treg cells display a more constrained motility pattern than Th17 cells (Fig. 2 *E* and *F*). The directionality ratio, a measure of track straightness, decayed more rapidly in Treg cells than in Th17 cells, indicating that Treg cells turn more frequently than Th17 cells (Fig. 2G).

To better understand the differing motility behaviors of Treg and Th17 cells, we plotted mean track speed as a function of meandering index (track displacement/track length) to generate migration plots (30). Cells with distinct migratory properties were divided into four quadrants by setting cross-hairs at a mean track speed of 10 μm/min and a meandering index of 0.2 (Fig. 2H). About 20% of both Treg and Th17 cells follow confined, slow motility (Fig. 2H, lower left quadrant). Interestingly, more than half of Treg cells (60%) adopted confined, fast migratory behavior (Fig. 2H, upper left quadrant), whereas about 50% of Th17 cells followed meandering, fast trajectories (Fig. 2H, upper right quadrant; Fig. 2 *I* and *J*). At 28 DPI, both Treg cells and the
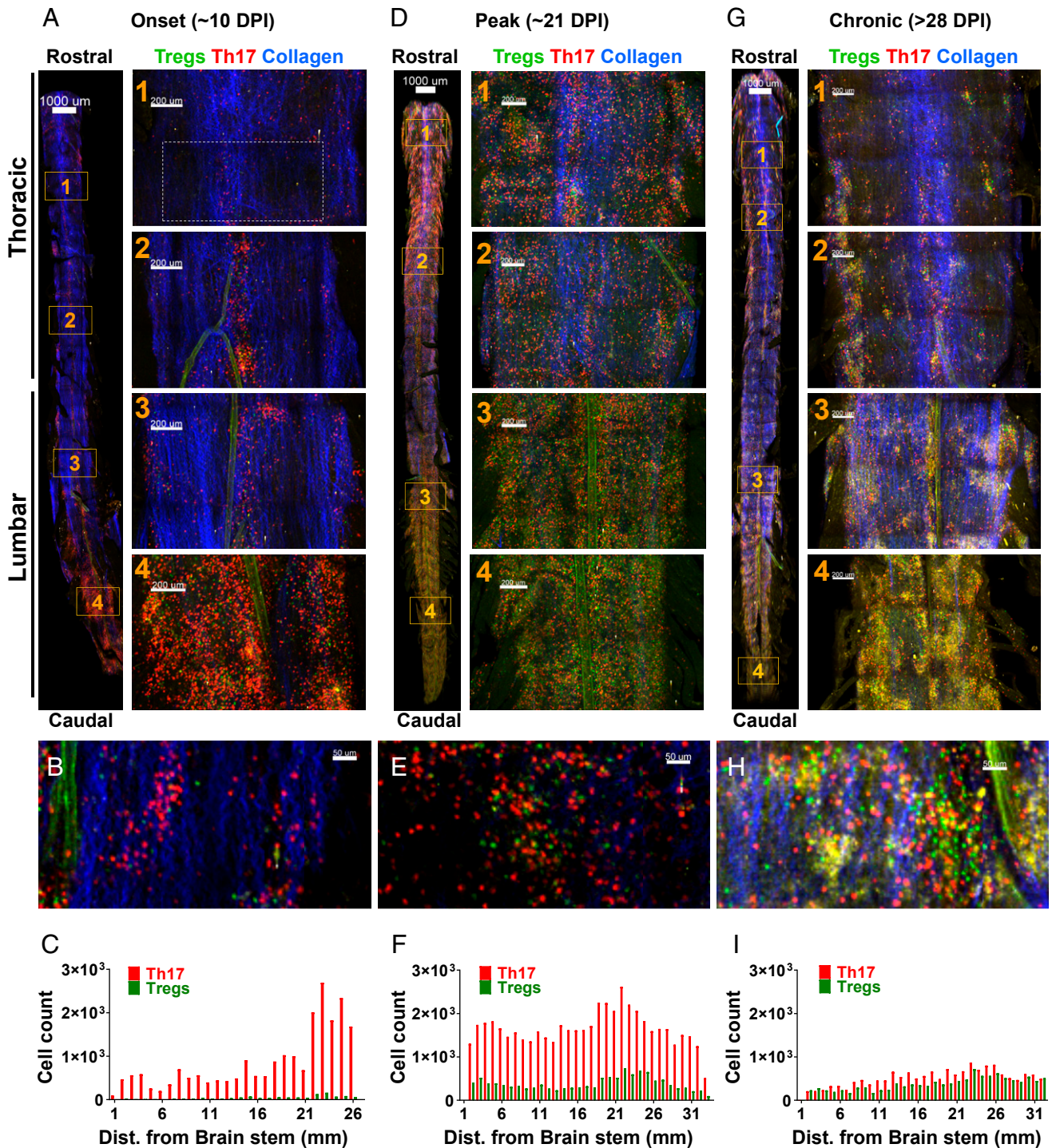
Fig. 1. Regional distribution of spinal cord-homing Treg and Th17 cells during EAE. EAE was induced in Foxp3^{EGFP} IL-17^{TdT} mice; spinal cords were isolated, paraformaldehyde-fixed at varying times of disease progression, and imaged by two-photon microscopy. Overview and corresponding magnified montage images of EAE spinal cords show localization of endogenous Treg and Th17 cells at the onset (*A–C*), peak (*D–F*), and chronic (*G–I*) phases of EAE in the ventral leptomeninges. Treg cells are in green, Th17 cells are in red, second harmonic signal from the collagen is in blue, and autofluorescent structures are in yellow. (Scale bars: overview, 1,000 μm; magnification, 200 μm.) (*Top*) Yellow rectangles *1* and *2* show thoracic regions; *3* and *4* show lumbar regions; dotted white rectangle marks untiled single-frame imaging area. (*Middle*) Distribution of Treg and Th17 cells in lumbar ventral cord at onset (*B*), peak (*E*), and chronic (*H*) phases of EAE. (*Bottom*) Histograms showing distributions of Th17 cells (red) and Treg cells (green) along the spinal cord at the onset (*C*), peak (*F*), and chronic (*I*) phases of EAE; number of cells (counts per millimeter length of cord) on the *y*-axis and their distance from the brainstem on the *x*-axis; data are representative of three independent EAE experiments (*SI Appendix,* Fig. S1 and Movies S1–S3).

remaining Th17 cells remained motile (*SI Appendix,* Fig. S2*A*). Trajectory analysis suggested that the differing motility patterns of Treg and Th17 cells are preserved during the chronic phase of EAE (*SI Appendix,* Fig. S2 *B–J*). Notably, instantaneous velocities and motility coefficients of Treg cells were similar to those at the peak (21 DPI), but Th17 cells on day 28 showed 35% higher
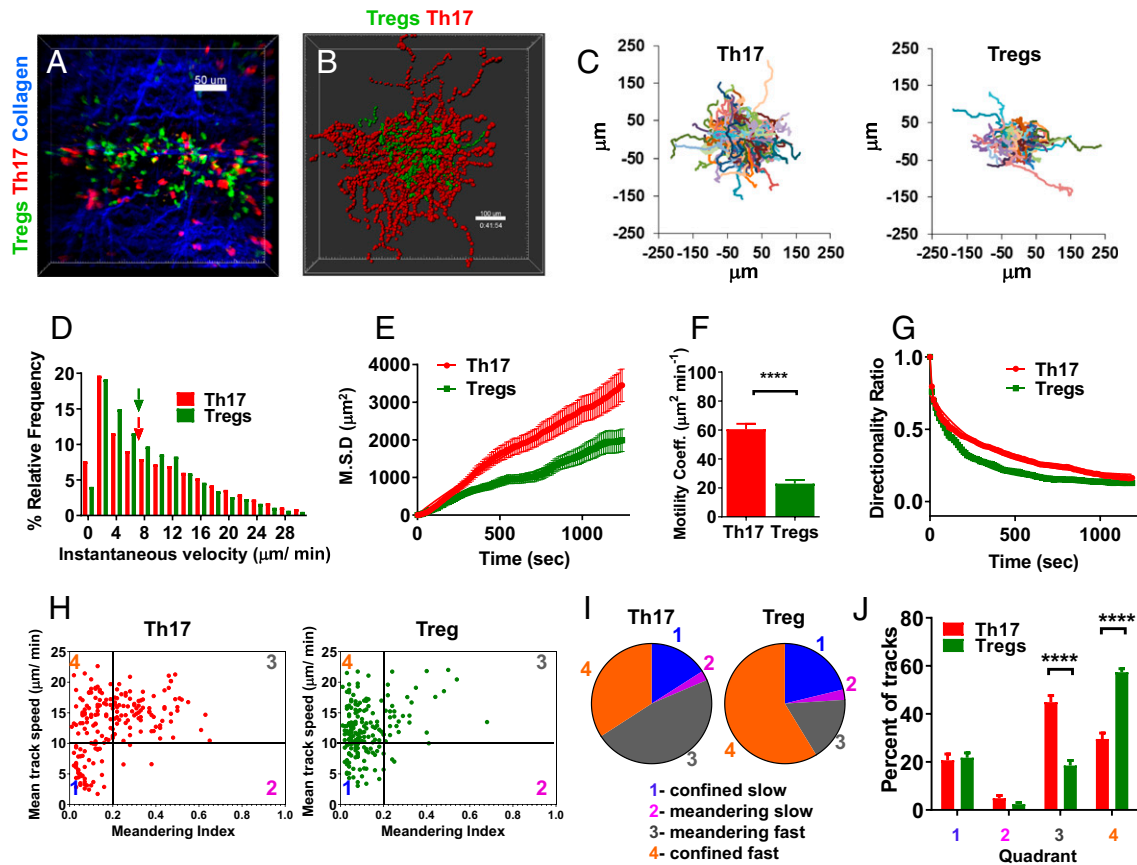
Fig. 2. Motility of endogenous Th17 and Treg cells in the spinal leptomeninges at the peak of EAE. EAE at peak (21 DPI) in Foxp3^EGFP IL-17^TdT mice; two-photon microscopy in explanted spinal cords. (*A*) Representative image showing Th17 cells (red), Treg cells (green), and collagen fibers (blue) in the meninges. (Scale bar, 50 μm.) (*B*) Three-dimensional spread of Treg cells (green spheres) and Th17 cells (red spheres). Spots are superimposed and origins normalized to the starting point. (Scale bar, 100 μm.) (*C*) Tracks of Treg and Th17 cells ($n > 194$ tracks, each track >20 min, 6 imaging fields, 2 independent experiments). (*D*) Instantaneous 3D velocity histograms for Th17 cells (575 tracks) and Treg cells (450 tracks); arrows indicate median: 7.5 vs. 7.1 μm/min, respectively ($n \geq 25,379$ measurements, 6 imaging fields, 2 independent experiments). (*E*) Mean squared displacement (MSD) over time for Th17 and Treg cells ($n > 190$ tracks, 6 imaging fields, 2 independent experiments). (*F*) Measured 3D motility coefficients (M = MSD/6t) for Treg and Th17 cells ($n \geq 450$ tracks each, 11 imaging sessions; ****$P < 0.0001$). (*G*) Directionality ratios (displacement/distance) as a function of time for Treg and Th17 cells (≥ 102 ratio measurements per time point, 6 imaging fields, 2 independent experiments). (*H*) Mean track speeds of Treg and Th17 cells plotted against meandering index (track displacement/track length). Each dot represents an individual T cell. Cross-hairs define four color-coded types of cell migration: *1*, confined, slow; *2*, meandering, slow; *3*, meandering, fast; and *4*, confined, fast. (*I*) Corresponding percent of tracks in each quadrant. (*J*) Quadrant analysis from *H* and *I* showing Th17 and Treg cell migration types ($n > 16$ imaging fields, 4 independent experiments; ****$P < 0.0001$, two-way ANOVA with Šidák multiple comparisons test; *SI Appendix*, Fig. S2 and Movie S4).

mean instantaneous 3D velocities (*SI Appendix*, Fig. S2*D*), with a correspondingly higher motility coefficient (*SI Appendix*, Fig. S2*F*).

In summary, Treg and Th17 cells display divergent motility patterns during EAE. Th17 cells actively spread along leptomeninges, where their presence leads to neuroinflammation across the spinal cord. In contrast, Treg cells are highly motile but spatially restrained by confined patterns of motility.

Adoptively Transferred Myelin-Specific Th17 Cells Recognize Autoantigens in the Spinal Cord. Effector T cell reactivation mediated by perivascular APCs potentiates autoimmune neuroinflammatory diseases (31, 32). However, not all CNS-infiltrating endogenous T cells are specific for myelin during EAE (33–35). We therefore sought to identify bona fide neuroantigen-specific reactivation of effector T cells in the leptomeninges during EAE. Motility characteristics have been previously used as a readout of antigen recognition in lymph nodes, where naïve T cells encountering APCs decrease their speed and become arrested during TCR signaling (36). We adoptively transferred MOG$_{35-55}$ peptide-specific 2D2^DsRed-Th17 cells at 10 DPI into Foxp3^EGFP mice, resulting in peak EAE scores within 4 to 5 days. Two-photon imaging

revealed both round immotile and amoeboid migratory 2D2^DsRed-Th17 cells, along with motile Treg cells (Fig. 3*A* and Movie S5). The median instantaneous velocity of 2D2-Th17 cells was significantly lower than for Treg cells within the same experimental preparation (Fig. 3*B*), suggesting ongoing TCR activation, most likely through APCs presenting autoantigen in the spinal cord. The average 2D2-Th17 motility coefficient was 30% lower than endogenous Th17 cells at the same stage of EAE (cf., Fig. 2*F*), but still higher than coimaged endogenous Treg cells (Fig. 3*C*). We also compared track speeds of adoptively transferred 2D2-antigen-specific Th17 cells (Fig. 3*D*, blue) with track speeds of endogenous Th17 cells (Fig. 3*D*, red) and Treg cells (Fig. 3*D*, green) at onset, peak, and chronic phases of EAE. 2D2-Th17 cells on average migrated more slowly than endogenous Th17 cells, presumably due to antigen-specific interactions with APCs, but the similar peak track speeds indicate that their intrinsic capacity to migrate rapidly is unchanged. As EAE progresses, Th17 cells migrate more rapidly, although differences were not significant for Treg cells. Notably, we observed several instances of arrested, enlarged 2D2-Th17 cells undergoing mitosis (Fig. 3*E*), consistent with local expansion of encephalitogenic T cell numbers in the CNS, and further evidence for active autoantigen presentation in the spinal
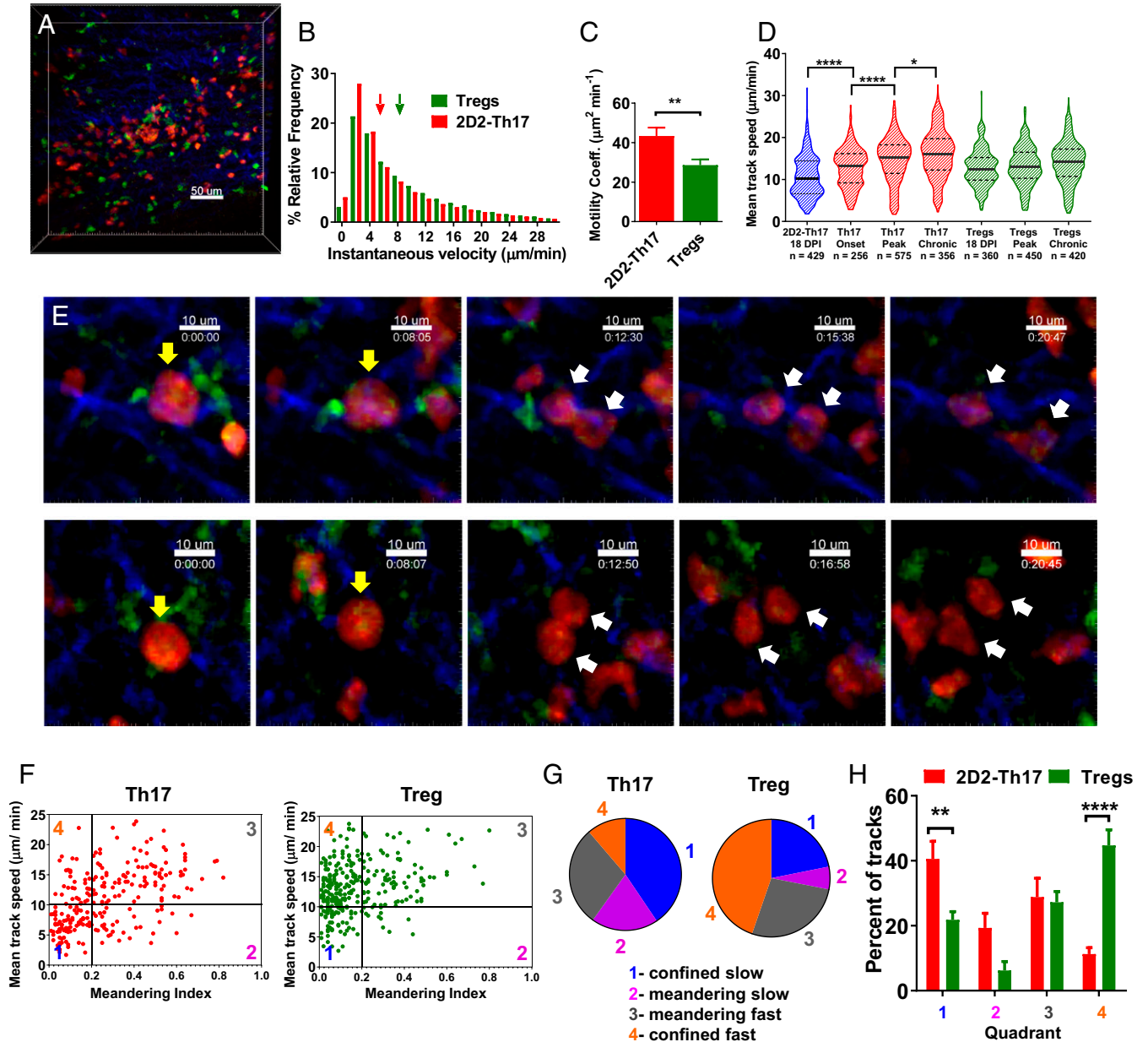
Fig. 3. Adoptively transferred MOG$_{35-55}$–specific Th17 cells recognize autoantigen and proliferate in the leptomeninges. EAE induced in Foxp3^{EGFP} mice, followed by adoptive transfer of in vitro-differentiated 2D2^{DsRed}-Th17 cells at day 10; spinal cords imaged at 18 DPI; EAE score = 3. (*A*) 2D2-Th17 cells (red), Treg cells (green), and collagen fibers (blue) in the lumbar leptomeninges. (Scale bar, 50 μm.) (*B*) Three-dimensional velocity histograms for 2D2-Th17 cells and Treg cells; arrows indicate median ($n \geq 48,928$ measurements, 9 imaging fields, 3 independent experiments, ****$P < 0.0001$). (*C*) Three-dimensional motility coefficients for 2D2-Th17 cells and Treg cells ($n \geq 288$ tracks, 5 imaging fields, 2 independent experiments; **$P = 0.0027$). (*D*) Mean track speeds of exogenous 2D2-Th17 cells 5 days after adoptive transfer (blue) compared to endogenous Th17 cells (red) and endogenous Treg cells (green). Solid and dotted lines indicate median and quartiles, respectively (****$P < 0.0001$, *$P = 0.02$, Kruskal–Wallis with Dunn's multiple comparisons test). (*E*) Cell division of two 2D2-Th17 cells (yellow arrows; white arrows point to daughter cells). Treg cells (green) and collagen fibers (blue); time in h:min:s. (Scale bar, 10 μm.) (*F*) Track speeds of 2D2-Th17 cells and Treg cells plotted against meandering index. (*G*) Corresponding charts of relative percentages of tracks in each quadrant. (*H*) Quadrant analysis from *F* and *G* showing the distribution of cell migration types ($n = 9$ imaging fields, 3 independent experiments; **$P < 0.01$, ****$P < 0.0001$, two-way ANOVA with Šidák multiple comparisons test; Movie S5).

cord. Quadrant analysis revealed that the proportion of 2D2-Th17 cells displaying a confined and slow motility—corresponding to a higher percentage of immotile cells that are undergoing TCR activation—was about twice that of endogenous Th17 cells (Fig. 3 *F–H*; cf., Fig. 2*J*). Notably, the fact that Treg cells maintained their confined and rapid motility, whether coimaged with endogenous Th17 cells (Fig. 2) or in the presence of an overwhelming excess of exogenous

2D2-Th17 cells, suggests that this mode of motility is intrinsic to Treg behavior in the spinal cord. Altogether, our results confirm that MOG$_{35-55}$–specific Th17 cells recognize autoantigens, proliferate, and disperse rapidly.

Treg Cells Engage APCs through Localized Repetitive Scanning Motility. Because Treg cells consistently displayed confined fast motility in

regions where many antigen-specific Th17 cells are proliferating, we hypothesized that both may interact with local APCs. To visualize CNS-APCs together with Treg cells, we imaged the spinal cords of Foxp3^{EGFP} CD11c^{EYFP} reporter mice after inducing EAE (37). Montage images of fixed spinal cords at 18 DPI revealed an organ-wide distribution of YFP$^+$ APCs (Fig. 4 *A* and *B*, bright yellow) and Treg cells (Fig. 4 *A* and *B*, green) along the caudal–rostral axis (Movie S6). Notably, most Treg cells were in close proximity to at least one APC (Fig. 4*C*). For live-cell imaging, we induced EAE in Foxp3^{EGFP} CD11c^{EYFP} reporter mice and adoptively transferred 2D2^{DsRed}-Th17 cells at 8 DPI. To assess whether Treg cells limit secondary activation of Th17 cells by inhibiting their interactions with APCs, we imaged the movement patterns of Treg cells and APCs together with MOG$_{35-55}$–specific Th17 cells at 13 DPI. Time-lapse microscopy revealed large YFP$^+$-APCs displaying typical dendritic cell morphology, while both GFP$^+$ Treg cells and 2D2-DsRed$^+$ Th17 cells appeared as typical elongated effector T cells (Fig. 4*D* and Movie S7). Cell bodies of APCs usually remained stationary while their dendrites actively probed the microenvironment; occasionally, we also observed migratory APCs. Importantly, we observed examples of Treg cells repetitively scanning the surface of an APC and displacing Th17 cells from APCs in the EAE spinal cord (Fig. 4*E* and Movie S7). Contacts between Treg cells and APCs on average lasted about 6 min, and some Treg cells interacted with APCs for more than 30 min (Fig. 4*F*). Furthermore, Treg cells engaged APCs for more than 50% of the total tracked time (Fig. 4*G*). Plotting displacement against time during sustained interactions revealed a characteristic back-and-forth oscillatory pattern (Fig. 4*H*), indicating that these Treg cells periodically revisit the same location. This "U-turn" behavior was repetitive, so that a Treg remained confined for several minutes, often in prolonged contact with an APC. We refer to this distinct Treg behavior as repetitive scanning motility (RSM). Based on the correlation between displacement at U-turn and revisit period for Treg cells during repetitive scanning (Fig. 4 *H* and *I*), we distinguish three variations of RSM (SI Appendix, Fig. S3 *A–C*): Treg cells moving a short distance and returning with high frequency, Treg cells moving an intermediate distance and returning with medium frequency, and Treg cells moving a large distance and returning with low frequency. On average, during repetitive scanning, Treg cells reversed direction of movement after migrating 10 μm, once every 5 min (Fig. 4 *J–L*). Consistent with these results, analysis of a duration-independent parameter—the directional persistence of cell tracks (38)—confirmed that coimaged 2D2-Th17 cells and endogenous Th17 cells migrated on straighter paths than did Treg cells (Fig. 4*M*). The turning behavior and directional persistence of individual Tregs imply that RSM is the cellular basis for the confined fast migration pattern of Treg cells at a population level (cf., Figs. 2*J* and 3*H*). In summary, long-lasting, dynamic RSM during Treg–APC interactions enable Tregs to efficiently scan the APC surface.

**Treg Cells Are Indispensable for the Resolution of Neuroinflammation.**
To determine the immunosuppressive effect of Treg cells in the spinal cord during autoimmune neuroinflammation, we induced a moderate form of EAE and depleted Treg cells in Foxp3^{DTR} mice that express diphtheria toxin (DT) receptor-enhanced green fluorescent (DTR-EGFP) fusion protein in Treg cells (39, 40) (SI Appendix, Fig. S4A). EAE progressively worsened following DT treatment, leading to an increase from 1 to 3 in the average clinical scores of Treg-depleted mice compared to PBS controls (SI Appendix, Fig. S4B). To assess the effect of Treg depletion on neuroinflammation, we analyzed the number of immune cells in spinal cords by flow cytometry. Seven days after Treg depletion, spinal cords of DT-treated mice harbored a threefold higher number of CD45$^+$ cells than in the control group (SI Appendix, Fig. S4 C and D). Depletion of Treg cells during EAE resulted in a substantial increase in the number of MHC-II–expressing CNS-APCs, with

little or no change in their mean fluorescence intensity (MFI) per cell (SI Appendix, Fig. S4 E–G). Moreover, Treg depletion led to a fourfold increase in number of costimulatory molecule-expressing APCs, but no change in mean CD80 and CD86 levels (SI Appendix, Fig. S4 H–M). Based on these results, we infer that the continued presence of Treg cells in the spinal cord helps to mitigate neuroinflammation in part by limiting the number of antigen-presenting cells.

**Th17 Cell Ca^{2+} Signals Are Diminished during the Established Phase of EAE When Many Treg Cells Are Present.** In vitro studies have shown that Treg cells suppress Ca^{2+} signaling in CD4$^+$ CD25$^-$ conventional T cells (41, 42), but whether this mechanism operates in vivo is not known. To monitor Th17 Ca^{2+} signaling in the spinal cord during EAE, we used a ratiometric genetically encoded Ca^{2+} indicator, Salsa6f (19) (Fig. 5 *A* and *B*). Salsa6f is a fusion protein in which TdTomato is linked to the Ca^{2+} indicator GCaMP6f by a V5 epitope tag. The [Ca^{2+}]-independent red fluorescence of the TdTomato moiety facilitates cell tracking, while the [Ca^{2+}]-dependent green fluorescence from GCaMP6f allows for real-time monitoring of cytosolic [Ca^{2+}]. Importantly, the GCaMP6f/TdTomato (G/R) ratio enables unambiguous determination of cytosolic Ca^{2+} levels independent of probe concentration or cell movement. We generated Foxp3^{EGFP} IL-17^{Salsa6f} transgenic mice that selectively express Salsa6f in Th17 cells and also express EGFP in Treg cells to simultaneously visualize endogenous Th17 and Treg cell dynamics and Th17^{Salsa} Ca^{2+} signaling in the leptomeninges during EAE progression (Fig. 5*C*). Our approach obviates the need for viral vectors to introduce the Ca^{2+} indicator, as done in previous studies using a rat adoptive transfer EAE model (17, 18). In addition, we developed image processing procedures to isolate Th17 cell fluorescence using cell masks and exclude green channel fluorescence from neighboring GFP-labeled Treg cells, as described in SI Appendix, Methods. These procedures enabled calculation of single-cell G/R ratios over time, with good signal to noise accurately reflective of Ca^{2+} levels in motile Th17^{Salsa} cells (Fig. 5*D* and SI Appendix, Fig. S5).

We then compared in situ Th17^{Salsa} cell Ca^{2+} signals in the spinal cord at the onset (10 to 14 DPI) and during established EAE (>21 DPI including both peak and chronic phases). At the onset of EAE, few if any Treg cells were visible (Fig. 5*E*), and episodes of Ca^{2+} signaling in Th17^{Salsa} cells were apparent. In RGB movies of Th17^{Salsa} cells, Ca^{2+} signals were recognized as increases in green fluorescence intensity (GCaMP) superposed on a stable red fluorescence (TdTomato), leading to transient changes in the apparent color of Salsa6f from red to orange and yellow (Movie S8). To evaluate the prevalence of Ca^{2+} signals, we mapped large-amplitude Ca^{2+} signals (G/R ratio >0.8) that arose during 20-min recording periods. In contrast to the numerous events observed at the onset of EAE (Fig. 5*F*), relatively few large Ca^{2+} transients were seen in Th17 cells during established EAE (Fig. 5 *G* and *H* and Movie S9). While the local density of Treg cells increased more than 100-fold from onset to established EAE, the density of Th17^{Salsa} cells in the same regions was unchanged (Fig. 5*I*). Therefore, the fewer large-amplitude Th17^{Salsa} Ca^{2+} transients (G/R > 0.8) observed during established EAE (Fig. 5*J*) resulted from less frequent Ca^{2+} signaling per cell, not a smaller number of Th17 cells. The mean Ca^{2+} level of Th17^{Salsa} cells from established EAE was also diminished relative to onset (Fig. 5*K*). Plotting the entire set of instantaneous Ca^{2+} levels as a frequency distribution revealed widespread suppression of Th17 Ca^{2+} signaling in the presence of Treg cells (Fig. 5*L*). Inspection of two-photon movies identified cells with moderately elevated [Ca^{2+}] in the cytosol that displayed rapid motility (SI Appendix, Fig. S5). During EAE onset, Ca^{2+} transients lasting 1 to 2 min were often observed in Th17^{Salsa} cells, either throughout the cell or localized to a small region, but were not tightly associated with changes in velocity (Fig. 5 *M* and *N*).
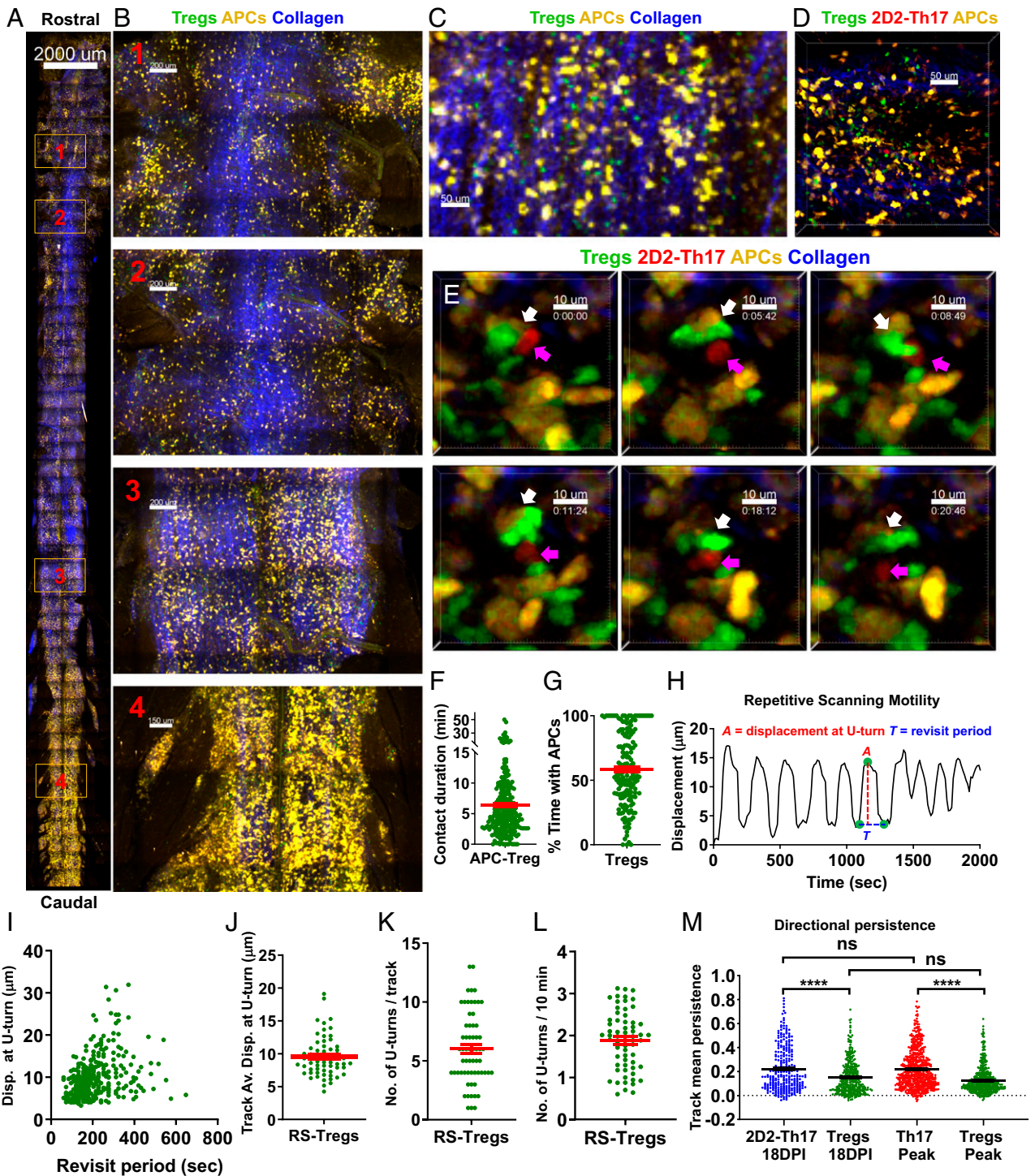
Fig. 4. Localization and choreography of Treg cells and antigen-presenting cells in the spinal cord. (*A* and *B*) Montage (*A*) and magnified images (*B*, *1* to *4*) of fixed EAE spinal cords illustrating Treg cells (green), CD11$^+$ APCs (yellow), and collagen second harmonic signal (blue) at 21 DPI from Foxp3^{EGFP} CD11c^{EYFP} mouse (representative of three independent EAE experiments). (Scale bars: *A*, 2,000 μm; *B*, 200 μm.) (*C*) Zoomed-in image from *A* showing association between Treg cells and APCs. (*D*) Representative image showing Treg cells (green), APCs (yellow), adoptively transferred 2D2-Th17 cells (red), and collagen (blue) in the lumbar region of EAE spinal cord from Foxp3^{EGFP} CD11c^{EYFP} mice, imaged live (13 DPI). (Scale bar, 50 μm.) (*E*) Cellular interactions in the EAE spinal cord (Movie S7); white arrows point to a Treg cell (green) scanning and physically displacing a 2D2-Th17 cell (red, magenta arrows) from an APC (yellow); collagen fibers in blue; time in h:min:s. (Scale bar, 10 μm.) (*F*) Contact durations between Treg cells and APCs (*n* = 255, 5 imaging fields, 2 independent experiments). (*G*) Percentage of time a tracked Treg is in contact with APC; symbols represent individual Treg tracks, red bars indicate mean ± SEM (*n* = 167, 3 imaging fields). (*H*) Example of Treg repetitive scanning behavior displayed as 3D displacement vs. time, and scheme for quantification of RSM as detailed in *Methods*. (*I*) Displacement at U-turn plotted as a function of revisit period (*r* = 0.42, Spearman's rank correlation; *P* < 0.0001, *n* = 367 pairs, 62 selected Treg cell tracks). (*J–L*) Summary of average cell displacement at U-turn for each track (*J*), number of U-turns per cell track (*K*), and frequency of U-turns (*L*). (*M*) Mean directional persistence for endogenous Treg cells (green) imaged together with either 2D2-Th17 cells (blue) or endogenous Th17 cells (red). Each symbol represents individual cell track, and black bars indicate mean ± SEM (****P < 0.0001, Kruskal–Wallis with Dunn's multiple comparisons test, *n* ≥ 9 imaging fields; *SI Appendix*, Fig. S3 and Movies S6 and S7).
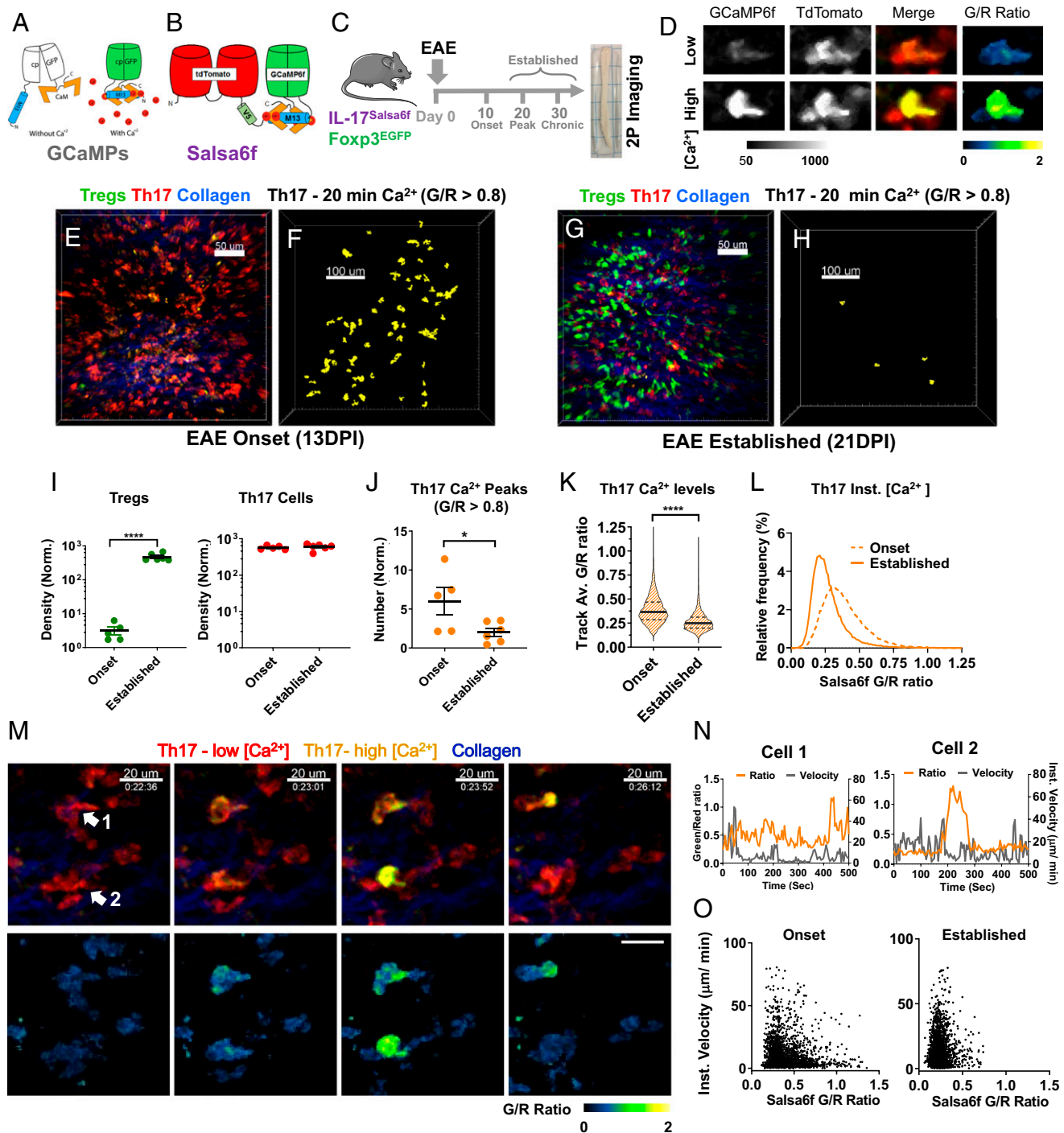
Fig. 5. Imaging in situ Th17 cell Ca²⁺ signaling during EAE. (*A* and *B*) Working principle of GCaMPs and Salsa6f. (*C*) Experimental design to visualize endogenous Treg and Th17 cells in the spinal cord of Foxp3^EGFP IL-17^Salsa6f mice. Spinal cords removed at 13 (score = 1), 21 (score = 3), and 28 (score = 1 to 2) DPI and imaged using two-photon microscopy. (*D*) Calculation of G/R ratio: Th17^Salsa cell with low and high [Ca²⁺] visualized in green (GCaMP6f) and red channels (TdTomato), as green/red merge, and (green/red) G/R ratio image. (*E*) Representative image from a time-lapse experiment showing Th17^Salsa cells at 13 DPI. (Scale bar, 50 μm.) (*F*) Corresponding cumulative map of Th17 Ca²⁺ signals over 20 min; thresholded cells in which all voxel G/R ratios were >0.8 are shown in yellow. (Scale bar, 100 μm.) (*G* and *H*) Corresponding image and cumulative map of Ca²⁺ signals in Th17^salsa cells at 21 DPI. (*I*) Treg and Th17^Salsa cell density (lumbar region) at onset (13 DPI) and in established (21–28 DPI) EAE. (*J*) Frequency of peak Ca²⁺ transients: signal with G/R ratio >0.8 normalized to the number of Th17^Salsa cells (*Methods*). For *I* and *J*, each symbol represents an imaging field (****P < 0.0001 for *I*, *P = 0.04 for *J*, unpaired *t* test, n = 5 to 6 imaging fields, 2 independent experiments). (*K*) Average Ca²⁺ level in each Th17^Salsa cell track. Solid and dotted lines indicate median and quartiles, respectively (n ≥ 3,360 tracks, ****P < 0.0001, n = 5 to 6 imaging fields). (*L*) Frequency distributions of all instantaneous G/R ratios (from cell tracks in *K*) at onset (dotted line, n = 79,550) and established EAE (solid line, n = 72,628). (*M*) Representative time sequence of Ca²⁺ signals in individual Th17^Salsa cells illustrating localized (cell 1) and cell-wide Ca²⁺ signals (cell 2) at 13 DPI (red/green merge, *Top*; G/R ratio, *Bottom*); time is shown in h:min:s. (Scale bar, 20 μm.) (*N*) Plots of Salsa6f G/R ratio (orange, left *y* axis) and corresponding instantaneous 3D velocity (gray, right *y* axis) for cells 1 and 2 in *M*. (*O*) Scatter plots of instantaneous 3D velocity and Salsa6f G/R ratio in Th17^Salsa cells at the onset (n = 2,407 pairs, r = −0.03, Spearman's rank correlation; P = 0.06) and in established EAE (n = 2,742 pairs, r = 0.02, Spearman's rank correlation; P = 0.21; *SI Appendix*, Fig. S5 and Movies S8 and S9).

Plotting of instantaneous cellular velocities with G/R ratios revealed a subpopulation of Th17 cells in which elevated $[Ca^{2+}]$ was compatible with rapid motility (Fig. 5O). In summary, these results indicate that Ca^{2+} signaling is prevalent in motile Th17 cells during EAE onset prior to the arrival of Treg cells, but is suppressed across the population of Th17 cells during the established phase of EAE when large numbers of Treg cells are present.

Treg Cells Suppress TCR-Induced Ca^{2+} Signaling in Th17 Cells. To determine the extent of Ca^{2+} signal suppression by Treg cells in the spinal cord, we monitored the frequency and duration of Ca^{2+} signals ex vivo in spinal cord-derived Th17^{Salsa} cells stimulated by plate-bound anti-CD3. As expected, preparations isolated at the onset of EAE showed few GFP$^+$ Treg cells, but many Th17^{Salsa} cells (red), nearly all of which exhibited robust Ca^{2+} responses (Fig. 6 A and B). In contrast, preparations isolated in the established phase of EAE included both Treg (green) and Th17^{Salsa} cells, and Ca^{2+} signals in Th17 ^{Salsa} cells were weaker (Fig. 6 C and D). Th17 cells in the established phase were also smaller compared to those at onset of EAE, suggestive of decreased activation state. Single-cell Ca^{2+} traces showed that Th17^{Salsa} cells isolated at the onset exhibited large, high-frequency Ca^{2+} signals (Fig. 6 E and F), whereas signals in cells isolated during established EAE were of smaller amplitude and lower frequency (Fig. 6 G and H). The average single-cell baseline, peak, and integrated Ca^{2+} levels of Th17^{Salsa} cells over time were all significantly lower in Th17^{Salsa} cells from established EAE (Fig. 6 I–K). The frequency distribution of instantaneous G/R ratios further demonstrates the overall reduction of TCR induced Ca^{2+} levels in Th17^{Salsa} cells from established EAE relative to onset (Fig. 6L). These ex vivo results are not only consistent with the suppression of endogenous Th17^{Salsa} cells in the spinal cord during established EAE (Fig. 5 J–L), but also indicate that Treg cells actively suppress anti-CD3 activated Th17^{Salsa} cells ex vivo. To examine whether the reduction of Ca^{2+} signals in Th17 cells during established EAE is due to down-regulation of SOCE (store-operated calcium entry), we treated cells with the SERCA pump inhibitor thapsigargin in Ca^{2+}-free solution to deplete ER Ca^{2+} stores and then restored extracellular Ca^{2+} to induce SOCE. Th17^{Salsa} cells isolated at both onset and established phases of EAE showed similar levels of SOCE (Fig. 6M), suggesting that the reduced Ca^{2+} signals in Th17 cells is not due to down-regulation of STIM and Orai function.

To address whether Treg cells directly suppress Th17 Ca^{2+} signals independent of APCs, we developed an in vitro assay to measure TCR-induced Ca^{2+} responses in in vitro-differentiated Th17^{Salsa} cells in the presence or absence of induced Treg cells. CD4$^+$ T cells obtained from FoxP3-GFP$^+$ mice were either differentiated into iTreg cells (green) or into control "non-Treg" cells that were negative for FoxP3 (non-green cells). Th17^{Salsa} cells were premixed with either iTreg or non-Treg cells for 1 h and plated onto anti-CD3–coated coverslips. While Ca^{2+} signals upon TCR stimulation were readily observed in Th17^{Salsa} cells alone and in Th17^{Salsa} cells cocultured with non-Treg cells, Th17^{Salsa} cells cocultured with iTreg cells showed significantly diminished Ca^{2+} signals (Fig. 6N). Statistical analysis showed that average single-cell baseline, peak, and integrated Ca^{2+} levels over time were all significantly lower in Th17 cells incubated with iTreg cells but not with control non-Treg cells (Fig. 6 O–Q). These results show that iTreg cells can directly suppress Ca^{2+} signaling in Th17 cells. Extrapolating these results to EAE, we conclude that spinal cord Treg cells ameliorate neuroinflammation by suppressing Th17 cell Ca^{2+} signaling and thus limiting Th17 cell reactivation.

Discussion

The interplay between proinflammatory Th17 cells and antiinflammatory Treg cells determines the progression and outcome of many autoimmune diseases (43, 44). We developed transgenic fluorescent reporter mouse strains to reliably label the entire populations of endogenous Th17 cells, Treg cells, and APCs in vivo, which enabled a comprehensive description of local movement patterns and physical interactions among these three cell types in the leptomeninges using two-photon microscopy. In addition, monitoring of Ca^{2+} in endogenous Th17 cells in situ using a genetically encoded Ca^{2+} indicator provided a continuous readout of activation state from single cells to entire local populations. Together, these approaches allowed us to systematically compare cell behavior and cell activation state and to define cellular mechanisms by which Treg cells restrain neuroinflammation in the spinal cord.

The lineage stability of Tregs and Th17 cells is heavily debated (43, 44). We acknowledge that a subset of cells expressing TdTomato under the IL-17ACre reporter may subsequently express IFNγ exclusively or concomitantly with IL-17 (22). For simplicity, we designate all TdTomato$^+$ T cells that currently or at some point in their history express IL-17 as Th17 cells. Similarly, genetic labeling with eGFP expressed under the FoxP3 promoter allowed us to identify endogenous bona fide Treg cell populations and to avoid adoptive transfer of iTreg cells that are known to rapidly lose Foxp3 expression in vivo (45). The Foxp3^{EGFP} IL-17^{TdT} transgenic mouse strain allowed us to image and attribute functions to populations of endogenous Treg and Th17 cells. In addition, Foxp3^{EGFP} CD11c^{EYFP} dual-reporter mice revealed cellular interactions, including repetitive scanning motility of Treg cells scanning the surface of APCs for prolonged periods, and Foxp3^{EGFP} IL-17^{Salsa6f} transgenic mice allowed Ca^{2+} signaling to be monitored in endogenous Th17 cells as they competed with Treg cells for space on APCs. These fate-mapped reporter mice permitted tracking of individual cells in endogenous populations while avoiding the use of adoptively transferred cells that can alter clinical progression.

Our live-cell imaging studies reveal the distribution of immune cells in relation to the sequence of clinical signs during the progression of EAE (*SI Appendix*, Fig. S6A), and strengthen the case that Th17 cells are primary mediators of neuroinflammation in EAE. We find that disease onset and progression correlate with the arrival and distribution of numerous endogenous Th17 cells in the spinal cord. Th17 cells initially appear at the caudal end of the spinal cord, a distribution mirroring tail paralysis at the onset of clinical signs. At the onset of clinical symptoms, Th17 cellular activation, as revealed by Ca^{2+} imaging, is elevated and subsequently declines as disease severity lessens. Adoptive transfer of MOG-specific Th17 cells confirms that the cellular environment of the spinal cord at the onset of EAE stimulates antigen-specific Th17 cell activation and proliferation, and this is associated with worsening clinical outcome. Moreover, Th17 cells increase in number and become more uniformly distributed throughout the cord at the peak of disease, paralleling the onset of quadriplegia. Whereas we focused on the leptomeninges as the region of primary interest for immune activation and regulation (25, 46–48), others have identified direct interactions between Th17 cells and spinal cord axons that lead to demyelination and neuronal damage (49). Th17 cells also aid in the formation of ectopic lymphoid follicles that sustain tissue inflammation (50). The rapid and apparently random local movements of Th17 cells we observe point to a capacity to spread rapidly through CNS tissue while promoting repeated local pathogenic interactions. Similar random-walk motility patterns may allow Th1 or Th17 cells to efficiently detect and mount rapid responses to bacterial and fungal infections (25, 51, 52). During the chronic phase of EAE, when tail paralysis and hind limb weakness persist, Th17 cells remain predominantly in the lumbar region although their overall number decreases. Altogether, our experiments support a local, direct, and continuing role for Th17 cells in immune-mediated neuronal damage in EAE.

Pathogenic activation of Th17 cells is reduced upon Treg entry into the spinal cord. In agreement with other studies (40, 53), our depletion experiments demonstrate that Treg cells limit disease progression and neuroinflammation in EAE. Treg cells, but not Th17 cells, display confined fast motility, while physical interactions
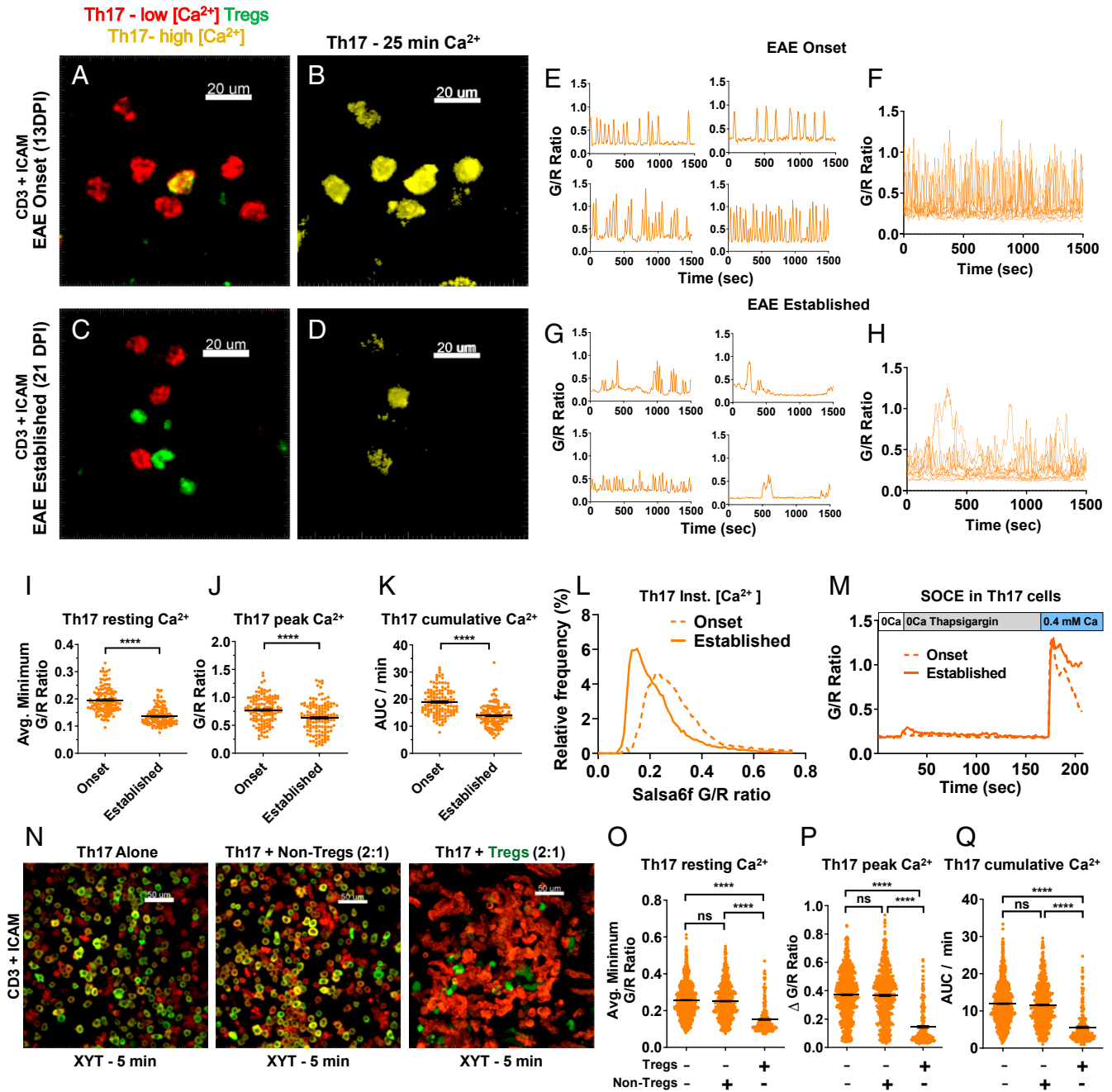
Fig. 6. TCR-activated Ca^{2+} signals in Th17 cells. (*A–M*) Th17^{Salsa} and Treg cells isolated from the spinal cord of Foxp3^{EGFP} IL-17^{Salsa6f} mice during onset (13 DPI) and established EAE (>21 DPI) and plated on anti-CD3 and ICAM-Fc–coated coverslips. (*A*) Representative confocal image showing Th17^{Salsa} cells at 13 DPI. (Scale bar, 20 μm.) Yellow cell shows a cell-wide Ca^{2+} transient. (*B*) Red and green channel overlay time-projection image from *A* showing Th17 Ca^{2+} signals over a 25-min recording period. (*C* and *D*) Same as *A* and *B*, but for cells from 21 DPI. Treg cells are constant green. (*E* and *F*) Representative single-cell G/R ratios (*E*) and overlay of several single-cell Th17^{Salsa} Ca^{2+} traces (*F*) during onset of EAE. (*G* and *H*) Corresponding traces for established EAE (*n* = 11 cells each for overlay trace shown in *F* and *H*). (*I–K*) Quantification of single-cell TCR-induced Th17^{Salsa} Ca^{2+} signals. Single-cell baseline Ca^{2+} levels (*I*), peak amplitude (*J*), and integrated (area under the curve) Ca^{2+} signal (*K*; ****P < 0.0001, *n* = 131 to 133 cells, ≥5 imaging fields, 2 independent experiments). (*L*) Frequency distributions of all G/R ratios in cells isolated at onset (dotted line, *n* = 42,239) and during established EAE (solid line, *n* = 41,909). (*M*) Average traces showing store-operated calcium entry (SOCE) in spinal cord-derived Th17^{Salsa} cells from onset and established EAE. The rates of rise of cytosolic Ca^{2+} signal (ΔG/R ratio in s^{-1}) following readdition of Ca^{2+}: onset, 0.127 ± 0.003; established EAE, 0.148 ± 0.004 (*n* = 32 to 90 cells, 3 imaging fields). (*N–Q*) iTreg cells suppress Ca^{2+} signals in in vitro-differentiated Th17 cells. (*N*) Overlay of green (GCaMP6f) and red channel (TdTomato) showing average Th17^{Salsa} Ca^{2+} signals over a 5-min time period (XYT). (Scale bar, 50 μm.) iTreg cells are identified by their constant green fluorescence without red, while control nonfluorescent non-Treg cells are identified in the bright-field channel (not depicted). (*O–Q*) Th17^{Salsa} single-cell baseline Ca^{2+} (*O*), peak Ca^{2+} (*P*), and integrated Ca^{2+} signal (*Q*; ****P < 0.0001, *n* = 205 to 780 cells, 3 independent imaging runs for each condition).

between Treg and Th17 cells are limited to brief encounters of passing cells, consistent with the lack of stable associations between Treg and T helper cells in diabetic pancreatic islets (54). We observed incoming Treg cells dispersed along the entire cord and occupying positions near pathogenic Th17 cells while interacting with APCs. In contrast to Th17 cell behavior, our observations show that Treg cells are confined while forming dynamic long-lasting contacts with CD11c$^+$ APCs and frequently adopt a back-and-forth motility pattern (repetitive scanning motility or RSM) in close association with APCs. We speculate that U-turns by Treg cells may arise from adhesive interactions with APC that are sufficiently strong to prevent detachment, but allow local exploration and surveillance. Possible mechanisms may include antigen-dependent TCR engagement that leads to confined migration with frequent turning reminiscent of "kinapses" (55), interaction between LFA-1 on Treg cells with its cognate ligand ICAM-1 on APCs (56), or interaction between CTLA-4 on Treg cells with CD80/86 costimulatory molecules on APCs (57). Given that nearly 50% of Treg cells in the spinal cord leptomeninges exhibited movement patterns classified as confined and fast, our data strongly suggest that RSM comprises a frequent and intrinsic part of the Treg behavioral repertoire. These specific, dynamic, yet long-lasting Treg–APC interactions may in turn provide repeated opportunities for local immune cell suppression (*SI Appendix*, Fig. S6*B*).

Other imaging studies in the skin have reported that Treg cells are immobile during homeostasis and show modest motility upon induction of inflammation (58). We have previously shown that, under homeostatic conditions in the lymph node, Treg cells migrate rapidly in the cortex, whereas follicular Treg cells migrate more slowly (37). Under inflammatory conditions, Treg cells formed prolonged contacts with DCs in the diffuse cortex of the lymph node (37, 56, 59), but did not display RSM as reported here for Treg cells in the EAE spinal cord. Unstable interactions between adoptively transferred antigen-specific Treg cells and tumor APCs were also reported in a tumor model (60). Thus, Treg cells display distinct tissue-specific modes of motility determined by inflammatory cues.

Distinctive cell behaviors imply specialized cell functions. Our live imaging of Treg and Th17 cells during established EAE suggests and constrains possible cellular mechanisms of Th17 cell suppression. Despite the potent and population-wide effects of Treg cells on Th17 cells, these cell types do not form long-term contacts, as have been observed for motile cognate T and B cell pairs at B cell follicles in the lymph node (61) and for tolerogenic (LPS-activated) B cells interacting with antigen-specific T cells during B cell-induced peripheral tolerance (38). In spinal cord during EAE, APCs may provide the platform on which Treg cells can modulate Th17 cell activation. We also found that Treg depletion leads to a substantial increase in APCs during EAE, possibly due to unchecked influx and expansion in situ, providing more opportunities for Th17 cell reactivation in the inflamed spinal cord. Real-time measurement of [Ca^{2+}] levels is a functional readout of Th17 cells accessing APCs. Diminished Th17 cell [Ca^{2+}] and increased velocities in the presence of Treg cells further support the observation of decreased Th17 cell–APC contacts. In addition, we observed instances of dissociation of APC–Th17 cell complexes in the presence of Treg cells.

In analyzing the relationship between Th17 cell Ca^{2+} signals and their motility characteristics, we found that many endogenous Th17 cells are able to actively migrate in the leptomeninges at the onset of EAE despite elevated [Ca^{2+}] levels, in contrast to the behavior of naïve T cells in lymph nodes, which stop when [Ca^{2+}] rises (13, 18, 36). These results agree with conclusions from adoptive-transfer EAE studies that compared antigen activation in lymph node or spleen and in spinal cord leptomeninges (17, 18). The difference in behavior may imply that autoreactive Th17 cells in the CNS have a higher Ca^{2+} threshold for stopping than naïve antigen-specific T cells in secondary

lymphoid organs. Our observations further raise the possibility that Th17 cell reactivation in situ may occur through kinapses in which T cells remain motile and exhibit Ca^{2+} signals while contacting APCs (55, 62, 63).

Our results point to possible strategies of therapeutic intervention for immune-mediated demyelination in multiple sclerosis. We demonstrate a direct suppression of TCR-induced Ca^{2+} signaling in Th17 cells by iTreg cells in vitro. The arrival and maintained presence of Treg cells in the spinal cord coincides with suppression of Ca^{2+} signaling across a large portion of the Th17 cell population in situ. This suppression of Ca^{2+} signaling persists when Th17 cells are removed from the spinal cord and stimulated ex vivo. Although the molecular mechanism for signal disruption remains uncertain, our results reinforce the therapeutic potential of Treg-based intervention strategies for autoimmune diseases. At the onset of EAE, Th17 cells in the leptomeninges exhibit continuous elevation of baseline Ca^{2+} levels in the cytoplasm that appears unrelated to the infrequent appearance of much larger transient Ca^{2+} signals. Elevation of Ca^{2+} implies activation of Ca^{2+} channels such as Orai1, which have been pharmacologically targeted to reduce Th17 cell activation and ameliorate EAE (16). The lag between the entry of Treg and Th17 cells into the EAE spinal cord points to an opportunity for Treg-based adoptive cell therapies to increase the flux of Treg cells into the site of neuroinflammation.

Materials and Methods

EAE Induction in Dual-Reporter Mouse Strains. All mice were housed in a clean, specific pathogen-free facility at the University of California, Irvine. Animal care and protocols were reviewed and approved by the institutional animal care and use committee of UCI (IACUC protocol AUP-18-176). Both male and female mice from the C57BL/6 background were used at 8 to 12 wk of age. We generated a Foxp3^{EGFP} IL-17^{Cre} strain by crossing Foxp3-EGFP reporter (64) and IL-17A-Cre fate-reporter mice (22). Foxp3^{EGFP} IL-17^{Cre} mice were subsequently crossed with loxP-flanked STOP (LSL) cassette-tdTomato Ai14 reporter (65) or with LSL-Salsa6f calcium-reporter mice (19) to generate Foxp3^{EGFP} IL-17^{TdT} and Foxp3^{EGFP} IL-17^{Salsa6f} mice, respectively. The *Il17a* locus in these Treg, Th17 dual-reporter mice was maintained in a hemizygous state so that one functional allele of the *Il17a* gene is available for the secretion of IL17A, while the other mutant allele encoding Cre-recombinase activates TdTomato or Salsa6f expression at the *Rosa26* locus. Foxp3^{EGFP} CD11c^{EYFP} mice were obtained by crossing Foxp3-EGFP reporter and Itgax-EYFP reporter mice (66). Active EAE was induced in mice by immunization with MOG$_{35-55}$ peptide emulsified in complete Freund's adjuvant (CFA) supplemented with heat-killed *Mycobacterium tuberculosis*, as described in *SI Appendix, SI Methods*. Clinical scores were assessed daily in a blinded fashion according to the following scale: 0, no signs; 1, tail paralysis; 2, hind limb paresis; 3, hind limb paralysis; 4, tetraplegia; and 5, moribund.

Imaging Tregs and Th17 Cells in the Spinal Cord and In Vitro. We imaged fixed spinal cords to obtain maps of the cellular distribution of endogenous populations of Treg cells, Th17 cells, and APCs throughout the entire cord. We imaged live explanted spinal cords as described (67) to visualize cell motility, interactions, and Ca^{2+} signaling. All displayed images are maximum intensity projections. To examine Ca^{2+} signaling in vitro by confocal microscopy, we isolated cells from the spinal cords of Foxp3^{EGFP} IL-17^{Salsa6f} mice at the onset of clinical signs (10 to 14 DPI) and during established EAE, including both peak and chronic phases (>21 DPI), and plated them on coverslips coated with anti-CD3, ICAM, and collagen. For in vitro Th17 Ca^{2+} assays, Th17^{Salsa} cells, FoxP3-GFP$^+$ induced Treg or iTreg cells, and control non-Treg cells were differentiated in vitro. iTreg or non-Treg cells were then mixed and incubated with Th17^{Salsa6f} cells at a 1:2 ratio 1 h prior to plating on activating surface of 2 µg/mL anti-CD3/2.5 µg/mL Fc-ICAM/collagen while maintaining 37 ± 0.5 °C temperature, 95% relative humidity, and 5% CO$_2$. Imaging was done 1 to 4 h after plating cells.

Data Analysis and Statistical Testing. GraphPad Prism (version 8.2.0) was used for generating figures and statistical analysis. *P* values, calculated by a nonparametric Mann–Whitney *U* test unless otherwise specified, are indicated in figures and legends. Details of specific statistical tests, numbers of replicates, and measures of variability are provided in the individual figure legends.

Data Availability. All data discussed in this paper are included in this article and the *SI Appendix*. The *SI Appendix* provides methodological details on EAE induction and Treg cell depletion, two-photon microscopy, confocal

1. S. Sakaguchi, T. Yamaguchi, T. Nomura, M. Ono, Regulatory T cells and immune tolerance. *Cell* **133**, 775–787 (2008).
2. T. S. Davidson, E. M. Shevach, Polyclonal Treg cells modulate T effector cell trafficking. *Eur. J. Immunol.* **41**, 2862–2870 (2011).
3. J. H. Esensten, Y. D. Muller, J. A. Bluestone, Q. Tang, Regulatory T-cell therapy for autoimmune and autoinflammatory diseases: The next frontier. *J. Allergy Clin. Immunol.* **142**, 1710–1718 (2018).
4. M. Gliwiński, D. Iwaszkiewicz-Grześ, P. Trzonkowski, Cell-based therapies with T regulatory cells. *BioDrugs* **31**, 335–347 (2017).
5. S. Z. Josefowicz, L. F. Lu, A. Y. Rudensky, Regulatory T cells: Mechanisms of differentiation and function. *Annu. Rev. Immunol.* **30**, 531–564 (2012).
6. K. Hirota, B. Martin, M. Veldhoen, Development, regulation and functional capacities of Th17 cells. *Semin. Immunopathol.* **32**, 3–16 (2010).
7. T. Korn, E. Bettelli, M. Oukka, V. K. Kuchroo, IL-17 and Th17 cells. *Annu. Rev. Immunol.* **27**, 485–517 (2009).
8. A. Amcheslavsky et al., Molecular biophysics of Orai store-operated Ca2+ channels. *Biophys. J.* **108**, 237–246 (2015).
9. M. D. Cahalan, STIMulating store-operated Ca(2+) entry. *Nat. Cell Biol.* **11**, 669–677 (2009).
10. P. A. Negulescu, N. Shastri, M. D. Cahalan, Intracellular calcium dependence of gene expression in single T lymphocytes. *Proc. Natl. Acad. Sci. U.S.A.* **91**, 2873–2877 (1994).
11. Y. Gwack, S. Feske, S. Srikanth, P. G. Hogan, A. Rao, Signalling to transcription: Store-operated Ca2+ entry and NFAT activation in lymphocytes. *Cell Calcium* **42**, 145–156 (2007).
12. P. A. Negulescu, T. B. Krasieva, A. Khan, H. H. Kerschbaum, M. D. Cahalan, Polarity of T cell shape, motility, and sensitivity to antigen. *Immunity* **4**, 421–430 (1996).
13. S. H. Wei et al., Ca2+ signals in CD4+ T cells during early contacts with antigen-bearing dendritic cells in lymph node. *J. Immunol.* **179**, 1586–1594 (2007).
14. S. Feske, CRAC channels and disease–From human CRAC channelopathies and animal models to novel drugs. *Cell Calcium* **80**, 112–116 (2019).
15. U. Kaufmann et al., Calcium signaling controls pathogenic Th17 cell-mediated inflammation by regulating mitochondrial function. *Cell Metab.* **29**, 1104–1118.e6 (2019).
16. U. Kaufmann et al., Selective ORAI1 inhibition ameliorates autoimmune central nervous system inflammation by suppressing effector but not regulatory T cell function. *J. Immunol.* **196**, 573–585 (2016).
17. N. I. Kyratsous et al., Visualizing context-dependent calcium signaling in encephalitogenic T cells in vivo by two-photon microscopy. *Proc. Natl. Acad. Sci. U.S.A.* **114**, E6381–E6389 (2017).
18. M. Mues et al., Real-time in vivo analysis of T cell activation in the central nervous system using a genetically encoded calcium indicator. *Nat. Med.* **19**, 778–783 (2013).
19. T. X. Dong et al., T-cell calcium dynamics visualized in a ratiometric tdTomato-GCaMP6f transgenic reporter mouse. *eLife* **6**, e32417 (2017).
20. C. S. Constantinescu, N. Farooqi, K. O'Brien, B. Gran, Experimental autoimmune encephalomyelitis (EAE) as a model for multiple sclerosis (MS). *Br. J. Pharmacol.* **164**, 1079–1106 (2011).
21. I. M. Stromnes, J. M. Goverman, Active induction of experimental allergic encephalomyelitis. *Nat. Protoc.* **1**, 1810–1819 (2006).
22. K. Hirota et al., Fate mapping of IL-17-producing T cells in inflammatory responses. *Nat. Immunol.* **12**, 255–263 (2011).
23. C. Caravagna et al., Diversity of innate immune cell subsets across spatial and temporal scales in an EAE mouse model. *Sci. Rep.* **8**, 5146 (2018).
24. O. Uckermann et al., Endogenous two-photon excited fluorescence provides label-free visualization of the inflammatory response in the rodent spinal cord. *BioMed Res. Int.* **2015**, 859084 (2015).
25. C. Schläger et al., Effector T-cell trafficking between the leptomeninges and the cerebrospinal fluid. *Nature* **530**, 349–353 (2016).
26. Y. Arima et al., Regional neural activation defines a gateway for autoreactive T cells to cross the blood-brain barrier. *Cell* **148**, 447–457 (2012).
27. S. Kretschmer et al., Autofluorescence multiphoton microscopy for visualization of tissue morphology and cellular dynamics in murine and human airways. *Lab. Invest.* **96**, 918–931 (2016).
28. M. Mitsdoerffer, A. Peters, Tertiary lymphoid organs in central nervous system autoimmunity. *Front. Immunol.* **7**, 451 (2016).
29. T. Korn et al., Myelin-specific regulatory T cells accumulate in the CNS but fail to control autoimmune inflammation. *Nat. Med.* **13**, 423–431 (2007).
30. P. Mrass et al., CD44 mediates successful interstitial navigation by killer T cells and enables efficient antitumor immunity. *Immunity* **29**, 971–985 (2008).
31. N. Kawakami et al., The activation status of neuroantigen-specific T cells in the target organ determines the clinical outcome of autoimmune encephalomyelitis. *J. Exp. Med.* **199**, 185–197 (2004).
32. A. Flügel et al., Migratory activity and functional changes of green fluorescent effector cells before and during experimental autoimmune encephalomyelitis. *Immunity* **14**, 547–560 (2001).
33. H. G. Lee et al., Pathogenic function of bystander-activated memory-like CD4+ T cells in autoimmune encephalomyelitis. *Nat. Commun.* **10**, 709 (2019).
34. F. Bischof et al., Analysis of autoreactive CD4 T cells in experimental autoimmune encephalomyelitis after primary and secondary challenge using MHC class II tetramers. *J. Immunol.* **172**, 2878–2884 (2004).
35. C. C. Lin et al., IL-1-induced Bhlhe40 identifies pathogenic T helper cells in a model of autoimmune neuroinflammation. *J. Exp. Med.* **213**, 251–271 (2016).
36. M. J. Miller, O. Safrina, I. Parker, M. D. Cahalan, Imaging the single cell dynamics of CD4+ T cell activation by dendritic cells in lymph nodes. *J. Exp. Med.* **200**, 847–856 (2004).
37. M. P. Matheu et al., Imaging regulatory T cell dynamics and CTLA4-mediated suppression of T cell priming. *Nat. Commun.* **6**, 6219 (2015).
38. M. P. Matheu et al., Toll-like receptor 4-activated B cells out-compete Toll-like receptor 9-activated B cells to establish peripheral immunological tolerance. *Proc. Natl. Acad. Sci. U.S.A.* **109**, E1258–E1266 (2012).
39. K. Lahl et al., Selective depletion of Foxp3+ regulatory T cells induces a scurfy-like disease. *J. Exp. Med.* **204**, 57–63 (2007).
40. M. Koutrolos, K. Berer, N. Kawakami, H. Wekerle, G. Krishnamoorthy, Treg cells mediate recovery from EAE by controlling effector T cell proliferation and motility in the CNS. *Acta Neuropathol. Commun.* **2**, 163 (2014).
41. A. Schmidt et al., Human regulatory T cells rapidly suppress T cell receptor-induced Ca(2+), NF-κB, and NFAT signaling in conventional T cells. *Sci. Signal.* **4**, ra90 (2011).
42. A. Schwarz et al., Fine-tuning of regulatory T cell function: The role of calcium signals and naive regulatory T cells for regulatory T cell deficiency in multiple sclerosis. *J. Immunol.* **190**, 4965–4970 (2013).
43. S. Sakaguchi, D. A. Vignali, A. Y. Rudensky, R. E. Niec, H. Waldmann, The plasticity and stability of regulatory T cells. *Nat. Rev. Immunol.* **13**, 461–467 (2013).
44. L. Zhou, M. M. Chong, D. R. Littman, Plasticity of CD4+ T cell lineage differentiation. *Immunity* **30**, 646–655 (2009).
45. S. Floess et al., Epigenetic control of the foxp3 locus in regulatory T cells. *PLoS Biol.* **5**, e38 (2007).
46. S. Pol et al., Characterization of leptomeningeal inflammation in rodent experimental autoimmune encephalomyelitis (EAE) model of multiple sclerosis. *Exp. Neurol.* **314**, 82–90 (2019).
47. J. Kipnis, Multifaceted interactions between adaptive immunity and the central nervous system. *Science* **353**, 766–771 (2016).
48. P. Kivisäkk et al., Localizing central nervous system immune surveillance: Meningeal antigen-presenting cells activate T cells during experimental autoimmune encephalomyelitis. *Ann. Neurol.* **65**, 457–469 (2009).
49. V. Siffrin et al., In vivo imaging of partially reversible th17 cell-induced neuronal dysfunction in the course of encephalomyelitis. *Immunity* **33**, 424–436 (2010).
50. A. Peters et al., Th17 cells induce ectopic lymphoid follicles in central nervous system tissue inflammation. *Immunity* **35**, 986–996 (2011).
51. S. Dusi et al., LFA-1 controls Th1 and Th17 motility behavior in the inflamed central nervous system. *Front. Immunol.* **10**, 2436 (2019).
52. Y. Li et al., The immunoregulation of Th17 in host against intracellular bacterial infection. *Mediators Inflamm.* **2018**, 6587296 (2018).
53. M. J. McGeachy, L. A. Stephens, S. M. Anderton, Natural recovery and protection from autoimmune encephalomyelitis: Contribution of CD4+CD25+ regulatory cells within the central nervous system. *J. Immunol.* **175**, 3025–3032 (2005).
54. Q. Tang et al., Visualizing regulatory T cell control of autoimmune responses in nonobese diabetic mice. *Nat. Immunol.* **7**, 83–92 (2006).
55. H. D. Moreau et al., Signal strength regulates antigen-mediated T-cell deceleration by distinct mechanisms to promote local exploration or arrest. *Proc. Natl. Acad. Sci. U.S.A.* **112**, 12151–12156 (2015).
56. J. Chen et al., Strong adhesion by regulatory T cells induces dendritic cell cytoskeletal polarization and contact-dependent lethargy. *J. Exp. Med.* **214**, 327–338 (2017).
57. O. S. Qureshi et al., Trans-endocytosis of CD80 and CD86: A molecular basis for the cell-extrinsic function of CTLA-4. *Science* **332**, 600–603 (2011).
58. Z. Chow, S. N. Mueller, J. A. Deane, M. J. Hickey, Dermal regulatory T cells display distinct migratory behavior that is modulated during adaptive and innate inflammation. *J. Immunol.* **191**, 3049–3056 (2013).
59. J. Yan, B. Liu, Y. Shi, H. Qi, Class II MHC-independent suppressive adhesion of dendritic cells by regulatory T cells in vivo. *J. Exp. Med.* **214**, 319–326 (2017).
60. C. A. Bauer et al., Dynamic Treg interactions with intratumoral APCs promote local CTL dysfunction. *J. Clin. Invest.* **124**, 2425–2440 (2014).
61. T. Okada et al., Antigen-engaged B cells undergo chemotaxis toward the T zone and form motile conjugates with helper T cells. *PLoS Biol.* **3**, e150 (2005).
62. V. Mayya et al., Durable interactions of T cells with T cell receptor stimuli in the absence of a stable immunological synapse. *Cell Rep.* **22**, 340–349 (2018).
63. H. D. Moreau et al., Dynamic in situ cytometry uncovers T cell receptor signaling during immunological synapses and kinapses in vivo. *Immunity* **37**, 351–363 (2012).
64. D. Haribhai et al., Regulatory T cells dynamically control the primary immune response to foreign antigen. *J. Immunol.* **178**, 2961–2972 (2007).
65. L. Madisen et al., A robust and high-throughput Cre reporting and characterization system for the whole mouse brain. *Nat. Neurosci.* **13**, 133–140 (2010).
66. R. L. Lindquist et al., Visualizing dendritic cell networks in vivo. *Nat. Immunol.* **5**, 1243–1250 (2004).
67. M. L. Greenberg et al., Two-photon imaging of remyelination of spinal cord axons by engrafted neural precursor cells in a viral model of multiple sclerosis. *Proc. Natl. Acad. Sci. U.S.A.* **111**, E2349–E2355 (2014).